ELSEVIER

Thermo-hydro-chemical couplings considered in safety assessment of shallow tunnels subjected to fire load

Matthias Zeiml[a],*, Roman Lackner[a,b], Francesco Pesavento[c], Bernhard A. Schrefler[c]

[a]*Institute for Mechanics of Materials and Structures, Vienna University of Technology, Karlsplatz 13/202, 1040 Vienna, Austria*
[b]*FG Computational Mechanics, Technical University of Munich, Arcisstr. 21, 80333 Munich, Germany*
[c]*Department of Structural and Transportation Engineering, University of Padua, Via F. Marzolo 9, 35131 Padua, Italy*

Abstract

Fire loading of concrete tunnel linings is characterized by various physical, chemical, and mechanical processes, resulting in spalling of near-surface concrete layers and degradation of strength and stiffness of the remaining tunnel lining. In this paper, the governing transport processes taking place in concrete at elevated temperatures are considered within a recently published fire-safety assessment tool [Savov K, Lackner R, Mang HA. Stability assessment of shallow tunnels subjected to fire load. Fire Safety J 2005; 40: 745–763] for underground structures. In contrast to consideration of heat transport only [Savov et al.], a coupled thermo-hydro-chemical analysis, simulating the heat and mass transport in concrete under fire loading, is performed, giving access to more realistic temperature distributions as well as gas-pressure distributions within the tunnel lining. These data serve as input for the structural safety assessment tool considering, in addition to the temperature dependence of mechanical properties, the effect of the gas pressure on the strength properties of the heated lining concrete. The combination of the two analysis tools (coupled analysis of governing transport processes and structural safety assessment) is illustrated by the fire-safety assessment of a cross-section of the Lainzer tunnel (Austria) characterized by low overburden (shallow tunnel).
© 2007 Elsevier Ltd. All rights reserved.

Keywords: Concrete; Fire; Spalling; Permeability; Polypropylene fibers; Tunnel lining; Layer concept; Level of loading; Collapse

1. Introduction

When concrete is subjected to elevated temperatures, various physical (e.g., evaporation, condensation, water and vapor advection, vapor diffusion, heat conduction and advection, phase expansion), chemical (e.g., dehydration, thermo-chemical damage), and mechanical (e.g., thermo-mechanical damage, cracking, spalling) processes take place. If this situation is simulated by means of an uncoupled thermal analysis, taking no mass transport into account, the temperature increase within the structure is significantly overestimated. This can be illustrated by comparing numerical with experimental results (see, e.g., [2]). This overestimation is explained by the neglect of (i) heat sinks associated with physical and chemical processes and (ii) the cooling effect in consequence of mass transport. This discrepancy between experimental data and numerical results obtained from uncoupled analyses as well as the need of safety-assessment tools for tunnels subjected to fire loading led to the development of more realistic models, considering heat and mass transport in a coupled manner [3–17]. Hereby, the governing equations are discretized in space by means of finite elements [3–7,11–16] or finite volumes [8–10,17] and are solved with respect to the primary state variables,[1] i.e.,

(1) the temperature T,
(2) the gas pressure p^g, and
(3) the capillary pressure[2] p^c [3–7].

*Corresponding author. Tel.: +43 1 58801 20240;
fax: +43 1 58801 20298.

E-mail addresses: matthias.zeiml@tuwien.ac.at (M. Zeiml),
Roman.Lackner@tuwien.ac.at (R. Lackner), pesa@dic.unipd.it
(F. Pesavento), bas@dic.unipd.it (B.A. Schrefler).

[1]The number of primary state variables is equal to the number of governing balance equations.
[2]The capillary pressure may be replaced by the saturation S_w [8–10], the vapor density ρ^{gw} [11], or the molar mass fraction of water vapor in gas [12,13].

Nomenclature

$\langle A \rangle_p$ localization tensor (dimensionless)

b slip-flow constant (Pa)

c_p specific heat capacity of concrete [kJ/(kg K)]

$c_p{}^{\mathrm{g}}$, $c_p{}^{\mathrm{w}}$ specific heat capacity of gas and water [kJ/(kg K)]

d thickness of tunnel lining (m)

d_{s} spalling depth (m)

d_{s}^{∞} final spalling depth (m)

$\mathbf{D}_{\mathrm{eff}}$ effective diffusivity of concrete (m^2/s)

E Young's modulus (MPa)

f_{c} compressive strength of concrete (MPa)

f_{t} tensile strength of concrete (MPa)

f_{y} yield stress of reinforcement steel (MPa)

f_r volume fraction of different phases in concrete (with $r \in \{$m… cement matrix, a… aggregates, l… liquid phase, g… gas phase$\}$) (dimensionless)

h specific enthalpy of vaporization (kJ/kg)

$\bar{K}$ stiffness of soil spring-element related to average radius of tunnel cross-section (N/m)

k_r bulk modulus of different phases in concrete (with $r \in \{$m… cement matrix, a… aggregates, l… liquid phase, g… gas phase$\}$) (MPa)

k_{int} intrinsic permeability of concrete (m^2)

$\mathbf{k}$, k absolute permeability of concrete (m^2)

k^{rg}, k^{rw} relative permeability of concrete to gas and water (dimensionless)

L level of loading (%)

$l_{\xi}{}^{\mathrm{w}}$ specific enthalpy of dehydration (kJ/kg)

$\dot{m}_{\mathrm{dehydr}}$ water source term due to dehydration [kg/(m^3 s)]

$\dot{m}_{\mathrm{vap}}$ water source term due to vaporization [kg/(m^3 s)]

M_{a}, M_{w}, M_{g} molar mass of air, water, and gas (kg/mol)

n porosity of concrete or number of finite elements (dimensionless)

p^{atm} atmospheric pressure (Pa)

p^{c}, p^{g} capillary and gas pressure (Pa)

p_0^{c}, p_0^{g} initial capillary and gas pressure (Pa)

$\bar{p}^{\mathrm{c}}$, $\bar{p}^{\mathrm{g}}$ prescribed capillary and gas pressure at inner surface of lining (Pa)

$p_{\mathrm{b}}^{\mathrm{c}}$ bubbling pressure (Pa)

p^{ga}, p^{gw} pressure of dry air and water vapor (Pa)

p_{∞}^{gw} prescribed vapor pressure of the surroundings (Pa)

p^{gws} saturation vapor pressure (Pa)

p^{w} water pressure (Pa)

p overpressure acting on porous network (concrete) (MPa)

q^{ga}, q^{gw} prescribed mass flux of dry air and water vapor [kg/(m^2 s)]

$q_{\mathrm{c}}^{\mathrm{gw}}$ convective mass flux of water vapor [kg/(m^2 s)]

q^{w} prescribed mass flux of water [kg/(m^2 s)]

q^T prescribed heat flux [kJ/(h m^2)]

q_{c}^T, q_{r}^T convective and radiative heat flux [kJ/(h m^2)]

r pore radius (m)

R radius of tunnel cross-section (m)

RH relative humidity of concrete (dimensionless)

S Eshelby tensor (dimensionless)

S_{w} degree of saturation (dimensionless)

S_{w0} initial degree of saturation (dimensionless)

$S_{\mathrm{w}}^{\mathrm{r}}$, $S_{\mathrm{w}}^{\mathrm{cr}}$ residual and critical degree of saturation (dimensionless)

t time (s)

T temperature (°C)

T_0 initial temperature (°C)

$\bar{T}$ prescribed temperature at inner surface of lining (°C)

T_{crit} critical temperature (°C)

T_{m}, ΔT equivalent temperature load (°C), (°C/m)

$\mathbf{u}$, u displacement of tunnel lining (m)

v vertical displacement at top of tunnel cross-section (m)

v_0 vertical displacement at top of tunnel cross-section at beginning of fire loading (m)

x horizontal coordinate (m)

x_k, x_{k0} actual and original coordinate of kth node (m)

y vertical coordinate (m)

α reduction factor for compressive strength of concrete (dimensionless)

α_T thermal expansion coefficient (1/°C)

β_{s} cubic thermal expansion coefficient of concrete (1/°C)

β_{c} convective mass-transfer coefficient (m/s)

λ thermal conductivity of concrete [kJ/(h m K)]

λ_{eff} effective thermal conductivity [kJ/(h m K)]

μ^{g}, μ^{w} dynamic viscosity of gas and water (Pa s)

v Poisson's ratio (dimensionless)

v_{m} Poisson's ratio of the cement matrix (dimensionless)

ρ, ρ_{c} apparent density of concrete (kg/m^3)

ρ^{s} solid-phase density (kg/m^3)

ρ^{g} gas density (kg/m^3)

ρ^{ga}, ρ^{gw} density of dry air and water vapor (kg/m^3)

ρ^{w} water density (kg/m^3)

$(\rho c_p)_{\mathrm{eff}}$ effective thermal capacity of concrete [J/(m^3 K)]

σ stress in reinforcement steel (MPa)

Σ macroscopic tensile stress in concrete (MPa)

ξ degree of hydration (dimensionless)

ξ_{dehydr} degree of dehydration (dimensionless)

In [3–7], the displacement field $\mathbf{u}$ is added to the list of primary state variables, allowing consideration of thermo-hydro-chemo-mechanical couplings. In contrast to the models formulated in [3–13], only the temperature T and the gas pressure p^{g} are used as primary state variables in [14–17].

In engineering practice, however, the highly non-linear temperature distributions in concrete members resulting from fire loading are commonly converted into (and replaced by) linear temperature distributions (given by the temperature T_m (°C) in the middle plane of the lining and a constant temperature gradient ΔT (°C/m) over the lining thickness). In contrast to the complex temperature distribution, T_m and ΔT can be easily considered in standard software tools developed for the (linear) analysis of beams and frames (see, e.g., [18,19]). The drawback of such a simplified structural analysis is two-fold. First, the stress state within the tunnel lining resulting from mechanical loading prior to temperature loading (i.e., self-weight of the lining and load of the surrounding soil) is not considered within the determination of the restraint forces due to thermal loading that lead to T_m and ΔT. Second, a linear-elastic analysis of the tunnel structure disregards stress redistribution due to the development of plastic regions within the structure. In order to avoid this questionable conversion of the temperature loading, analysis tools, taking the non-linear temperature distributions as well as plasticity of the lining material into account, have been developed (see, e.g., [1,20–23]).

Departing from the safety-assessment tool presented in [1], thermo-hydro-chemical couplings, based on the governing equations outlined in [3–7], are incorporated in this paper. The respective finite element (FE) formulation and its extension to prescribed spalling histories are outlined in Section 2. Section 3 contains a brief review of the structural "beam-spring" model presented in detail in [1], which is applied to a cross-section of the Lainzer tunnel (Austria), characterized by low overburden. The respective results are presented and discussed in Section 4.

2. Coupled thermo-hydro-chemical model

2.1. Finite element formulation

Within the proposed extension of the safety-assessment tool, concrete is treated as a multi-phase medium, consisting of solid, liquid (water), and gaseous (water vapor and dry air) phases. The governing macroscopic balance equations[3] are solved in a fully coupled manner with respect to the main state variables, i.e., capillary pressure p^c (Pa), gas pressure p^g (Pa), and temperature T (°C) [3–7]:

(1) Mass balance equation for the water phase (water vapor and liquid water, involving the solid mass balance equation):

$$n(\rho^w - \rho^{gw})\frac{\partial S_w}{\partial t} + n(1 - S_w)\frac{\partial \rho^{gw}}{\partial t} + nS_w\frac{\partial \rho^w}{\partial t}$$
$$- (1-n)\beta_s[\rho^{gw} + (\rho^w - \rho^{gw})S_w]\frac{\partial T}{\partial t}$$
$$- \text{div}\left(\rho^{gw}\frac{\mathbf{k}k^{rg}}{\mu^g}\text{grad }p^g\right) - \text{div}\left(\rho^w\frac{\mathbf{k}k^{rw}}{\mu^w}\text{grad }p^w\right)$$
$$- \text{div}\left[\rho^g\frac{M_a M_w}{M_g^2}\mathbf{D}_{\text{eff}}\text{grad}\left(\frac{p^{gw}}{p^g}\right)\right]$$
$$= -\frac{(1-n)[\rho^{gw}(1-S_w) + \rho^w S_w]}{\rho^s}\frac{\partial\rho^s}{\partial\xi}\frac{\partial\xi}{\partial t}$$
$$- [\rho^{gw}(1-S_w) + \rho^w S_w]\frac{\dot{m}_{\text{dehydr}}}{\rho^s} + \dot{m}_{\text{dehydr}}. \quad (1)$$

(2) Mass balance equation for the dry air phase (involving the solid mass balance equation):

$$- n\rho^{ga}\frac{\partial S_w}{\partial t} + n(1-S_w)\frac{\partial \rho^{ga}}{\partial t}$$
$$- \rho^{ga}(1-n)(1-S_w)\beta_s\frac{\partial T}{\partial t}$$
$$- \text{div}\left(\rho^{ga}\frac{\mathbf{k}k^{rg}}{\mu^g}\text{grad }p^g\right)$$
$$- \text{div}\left[\rho^g\frac{M_a M_w}{M_g^2}\mathbf{D}_{\text{eff}}\text{grad}\left(\frac{p^{ga}}{p^g}\right)\right]$$
$$= -\frac{(1-n)\rho^{ga}(1-S_w)}{\rho^s}\frac{\partial\rho^s}{\partial\xi}\frac{\partial\xi}{\partial t}$$
$$- \rho^{ga}(1-S_w)\frac{\dot{m}_{\text{dehydr}}}{\rho^s}. \quad (2)$$

(3) Enthalpy balance equation:

$$(\rho c_p)_{\text{eff}}\frac{\partial T}{\partial t}$$
$$- \left(\rho^g c_p^g\frac{\mathbf{k}k^{rg}}{\mu^g}\text{grad }p^g + \rho^w c_p^w\frac{\mathbf{k}k^{rw}}{\mu^w}\text{grad }p^w\right)\text{grad }T$$
$$- \text{div}(\lambda_{\text{eff}}\text{grad }T) = -\dot{m}_{\text{vap}}h - \dot{m}_{\text{dehydr}}l_\xi^w \quad (3)$$

with

$$\dot{m}_{\text{vap}} = -n\rho^w\frac{\partial S_w}{\partial t} - nS_w\frac{\partial \rho^w}{\partial t} + \rho^w(1-n)S_w\beta_s\frac{\partial T}{\partial t}$$
$$+ \text{div}\left(\rho^w\frac{\mathbf{k}k^{rw}}{\mu^w}\text{grad }p^w\right) - \frac{(1-n)\rho^w S_w}{\rho^s}\frac{\partial\rho^s}{\partial\xi}\frac{\partial\xi}{\partial t}$$
$$- \rho^w S_w\frac{\dot{m}_{\text{dehydr}}}{\rho^s} + \dot{m}_{\text{dehydr}}. \quad (4)$$

Eqs. (1)–(4) were obtained by introducing Darcy's law for pressure-driven flow of water and vapor, Fick's law for

---

[3]In contrast to [3–7] (i) gravitational effects were not considered, (ii) the sign of the mass source term associated with dehydration of the cement paste, $\dot{m}_{\text{dehydr}}$ [kg/(s m³)], was changed, and (iii) the dehydration process was described by the hydration degree ξ (dimensionless) instead of the degree of dehydration ξ_{dehydr} (dimensionless).

diffusional flow, and Fourier's law for heat conduction. Moreover, the following constitutive relations were employed:

- Kelvin–Laplace law (definition of the relative humidity RH (dimensionless)),
- Clausius–Clapeyron equation or Hyland–Wexler formula, relating the saturation-vapor pressure p^{gws} (Pa) to the temperature T (°C),
- Young–Laplace equation, relating the capillary pressure p^c (Pa) to the pore radius r (m),
- Clapeyron equation (ideal gas law), and
- Dalton's law (definition of partial pressures of water vapor, p^{gw} (Pa), and of dry air, p^{ga} (Pa)).

Additionally, the following relationships were determined from experimental data (for details, see Section 4.1):

- Degree of hydration ξ (dimensionless) versus temperature T (°C), with $\dot{\xi} < 0$ during heating, extracted from thermogravimetric measurements (see, e.g., [24]).
- Saturation S_w (dimensionless) versus capillary pressure p^c (Pa) and temperature T (°C) [25–29], which can be deduced from MIP or sorption-isotherm experiments.
- Intrinsic permeability k_{int} (m²) versus temperature T (°C), determined from permeability experiments [2].
- Relative permeabilities to water and gas (k^{rw} (dimensionless) and k^{rg} (dimensionless)) versus saturation S_w (dimensionless) [4,30–32], extracted from permeability experiments.

The boundary conditions (BC) within the employed FE formulation are defined by (i) prescribed values for the temperature ($\bar{T}$) and for the pressures ($\bar{p}^g$ and $\bar{p}^c$) (Dirichlet's BC), (ii) prescribed heat fluxes q^T and mass fluxes (q^{ga}, q^{gw}, and q^w) (Neumann's BC), or (iii) heat and mass transfer fluxes (Cauchy's BC) introducing heat and mass-transfer parameters (yielding convective and radiative heat flux, q_c^T and q_r^T, respectively, and convective water-vapor flux q_c^{gw}). The resulting set of governing equations is discretized in space and time and solved by means of a Newton–Raphson iteration scheme.

2.2. Consideration of spalling

In order to simulate heat and mass transport processes in case of spalling of the tunnel lining, the one-dimensional (1D) model[4] of the coupled FE formulation presented in the previous subsection is extended towards a moving boundary, representing the actual location of the spalling front, denoted as $d_s(t)$ (m) (see Fig. 1). Hereby, the FE nodes characterized by $x_i < d_s(t)$ are deactivated except for the closest node to the spalling front. This node (kth node in Fig. 1), however, is shifted to the actual location of the

---

4Based on the geometrical properties and the loading conditions found during tunnel fires, a 1D FE model is employed.
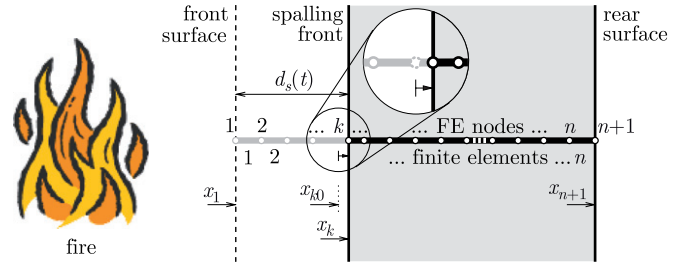

Fig. 1. One-dimensional FE model taking moving spalling front into account (n: number of finite elements, $d_s(t)$ (m): spalling depth, x_{k0} (m): original location of kth node).

spalling front, with $x_k = d_s(t)$, allowing us to consider spalling according to the prescribed spalling history. It is worth mentioning that, since spalling depends on numerous parameters (such as moisture content, heating rate, mechanical loading, etc.), the prediction of the risk and the amount of spalling is a very complex task and presently subject of intensive research. Within this paper, prescribed spalling histories are considered which were derived on basis of experimental observations/data collected within the fire experiments presented in [33].

3. Structural model for safety assessment of tunnel linings

The numerical model that is used to analyze tunnel structures mainly depends on the type of the surrounding soil and the depth of the tunnel [34]. For example, in case of tunnels with high overburden and/or in hard/medium-hard rock or highly cohesive soil, the load-carrying capacity of the surrounding soil is taken into account by plane-strain and 3D-FE models. In case of tunnels with low overburden and/or in soft soil (which are subject of this work), the load-carrying capacity of the surrounding soil is neglected by using a "beam-spring" model [35]. During fire loading, the soil loads the weakening tunnel support structure, which can cause its collapse.

Within the employed "beam-spring" model [1], the tunnel lining is represented by layered finite beam elements (see Fig. 2(a)). The layer concept enables consideration of (i) spalling of the tunnel lining by deactivation of the respective layers and (ii) assignment of temperature-dependent material parameters of concrete and reinforcement steel to the remaining layers. The beam elements are supported at the nodes by spring elements (see Fig. 2(b)). The stiffness $\bar{K}$ (N/m) of these springs is related to the specific subarea of the tunnel wall associated to the node, the Young's modulus E (MPa) of the surrounding soil, and its Poisson's ratio v (dimensionless) (for details, see [1]). In order to account for the zero load-carrying capacity of the soil under tensile loading, the stiffness of the spring elements is only activated when the spring is subjected to compressive loading. In case of tensile loading, $\bar{K}$ is set equal to zero. This enables for a realistic description of the behavior of the surrounding soil in case of low overburden

(a)

(b)

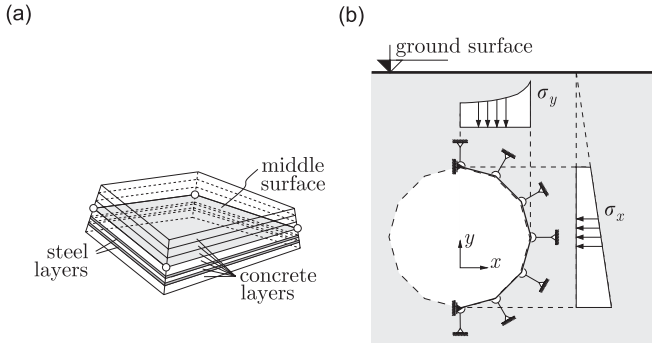

Fig. 2. Illustration of (a) layered finite beam element (containing concrete and steel layers) and (b) beam-spring model [1].
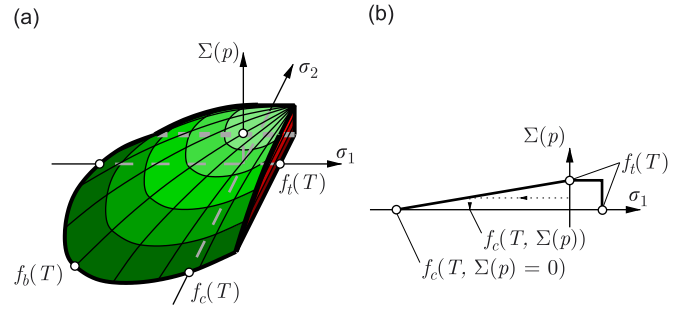
(a)

(b)

Fig. 3. (a) Consideration of out-of-plane tensile stress $\Sigma(p)$ within Drucker–Prager failure criterion for concrete, and (b) linear decrease of f_c with increasing out-of-plane loading.

and soft soil. The external load of the surrounding soil is applied at the FE nodes.

The mechanical behavior of concrete and steel is modeled by plane-stress elasto-plastic material models.[5] In case of concrete, a multi-surface plasticity model is used, with the Drucker–Prager and the Rankine criterion describing compressive and tensile failure, respectively (for details, see [1]). For description of the mechanical behavior of steel, a 1D model is used, referring to the strain component in the direction of the steel bars. In both cases, associative hardening plasticity is employed. Details on the employed failure criteria, the hardening laws and the temperature dependence of the material parameters can be found in [1]. The temperature dependence of strength and Young's moduli of concrete and steel are described by design curves according to international or national standards [36,37], giving, e.g., the compressive strength of concrete as

$$f_c(T) = f_c \cdot \alpha(T), \tag{5}$$

where $\alpha(T)$ (dimensionless) is a temperature-dependent coefficient, with $0 \leqslant \alpha(T) \leqslant 1$. Hereby, the reduction factor $\alpha(T)$ is correlated with the maximum temperature reached in a certain point of the structure during fire loading, hence, $f_c(T) = f_c(T_{max})$. In contrast to the safety-assessment tool presented in [1], tensile loading in the out-of-plane direction resulting from gas pressure within the pore space is considered within the plane-stress elasto-plastic material model for concrete (see Fig. 3). Taking into account the mainly biaxial compressive state of loading of the tunnel lining close to the heated surface, the effect of the out-of-plane loading by the gas pressure on the strength properties is considered by

$$f_c(T, p) = f_c \cdot \alpha(T) \cdot \left(1 - \frac{\Sigma(p)}{f_t(T)}\right), \tag{6}$$

where $\Sigma(p)$ (MPa) is the macroscopic tensile stress perpendicular to the heated surface, representing the overpressure

$p = p^g - p^{atm}$ (MPa) acting on the porous network, and $f_t(T)$ (MPa) is the temperature-dependent tensile strength of concrete (see, e.g., [36,37]). The macroscopic tensile stress $\Sigma(p)$ is related to p by the continuum-micromechanics approach outlined in [38], giving

$$\Sigma(p) = f_g \cdot p \cdot \langle A \rangle_p, \tag{7}$$

where $f_g = (1 - S_w)n$ (dimensionless) is the volume fraction of the gas phase subjected to pressure p (MPa) (with S_w (dimensionless) as the liquid saturation and n (dimensionless) as the porosity). $\langle A \rangle_p$ (dimensionless) represents the so-called localization tensor, reading for the case of spherical inclusions

$$\langle A \rangle_p = \left[(1 - S) \sum_r \frac{f_r}{1 + S \frac{k_r - k_m}{k_m}} \right]^{-1}, \tag{8}$$

where f_r (dimensionless) and k_r (MPa) are the volume fraction and the bulk modulus of the rth phase, respectively, with $r \in \{m \ldots \text{cement matrix}, a \ldots \text{aggregates}, l \ldots \text{liquid phase}, g \ldots \text{gas phase}\}$. In Eq. (8), S (dimensionless) represents the Eshelby tensor specialized for spherical inclusions, with $S = 1/3(1 + v_m)/(1 - v_m)$, where v_m (dimensionless) denotes Poisson's ratio of the cement matrix.

4. Application

The coupled analysis tool for the safety assessment of tunnels subjected to fire loading is used to investigate the performance of a cross-section of the Lainzer tunnel (Austria) (see Fig. 4(a)). Fig. 4(b) shows the cross-section of the lining in detail. The plastic mat (made of a layer of polyethylene laminated to a polypropylene (PP) mat) was installed prior to casting of the tunnel lining in order to ensure unrestrained movement of the tunnel lining along the shotcrete shell. During fire loading, this mat may act as an impermeable layer to water and vapor. On the other hand, gaps between the shotcrete shell and the concrete tunnel lining may allow the water and vapor to expand in the circumferential and/or longitudinal direction. In the numerical analysis, these two limiting cases are considered by prescribing the respective BC at the outside of the tunnel lining, i.e., (i) sealed and (ii) unsealed conditions.

---

[5]Because of the rather small thickness of the tunnel lining compared to the radius of the tunnel, the normal stress component perpendicular to the lining surface is set equal to zero.
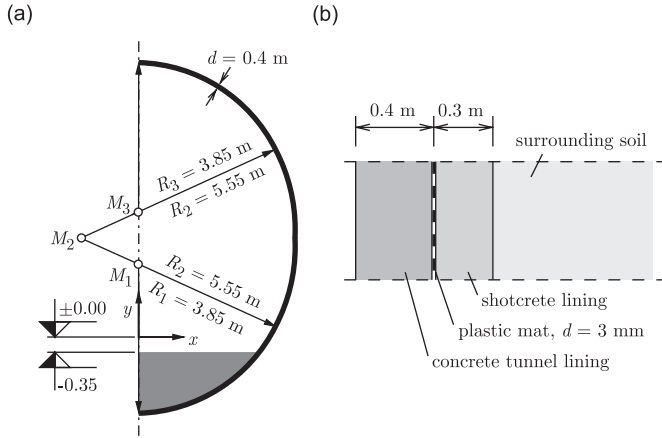
Fig. 4. Geometric properties of the considered cross-section of the Lainzer tunnel: (a) dimensions of the tunnel and (b) cross-section of the tunnel lining.

4.1. Material properties

Table 1 contains the input parameters for the coupled analysis (details on the mix design of the considered concrete can be found in [2]). The mechanical parameters of concrete and reinforcing steel used within the structural analysis are listed in Table 2.

4.1.1. Dehydration of heated concrete

The degree of hydration ξ (dimensionless), with $\xi = m_{\mathrm{h}}/m_{\mathrm{h0}}$ (where m_{h} (kg/m^3) is the actual amount of chemically-bound water and m_{h0} (kg/m^3) is the initial amount of chemically-bound water due to hydration that is present prior to heating), is defined as a function of temperature (see Fig. 5). This function, which can be extracted from thermogravimetric measurements (see, e.g., [24]), is used for determination of the rate of weight loss of water due to dehydration $\dot{m}_{\mathrm{dehydr}}$ [kg/(s m^3)] (see Eqs. (1)–(4)), defined as

$$\dot{m}_{\mathrm{dehydr}} = -m_{\mathrm{h0}} \frac{\partial \xi}{\partial t}. \tag{9}$$

It is worth mentioning that hydration of concrete is temperature-dependent and, in addition, also dependent on the relative humidity (i.e., the vapor pressure). However, the inversion of the hydration process in order to obtain the constitutive relation for dehydration is not straightforward. Because of lack of experimental data concerning the dependence of the dehydration process on the relative humidity, the dehydration process was described as a function of temperature only.

4.1.2. Saturation in heated concrete

According to [27], the saturation S_{w} (dimensionless) is related to the capillary pressure p^{c} (Pa) by

$$S_{\mathrm{w}} = \left[1 + \left(\frac{p^{\mathrm{c}}}{p_{\mathrm{b}}^{\mathrm{c}}} \right)^{1/(1-m)} \right]^{-m}, \tag{10}$$

the applicability to concrete of which was shown in [28,29]. In Eq. (10), $p_{\mathrm{b}}^{\mathrm{c}}$ (Pa) is the so-called bubbling pressure

(defined as the minimum value of p^{c} on a drainage capillary pressure curve, at which a continuous gas phase exists in the void space) and m (with $0 \leqslant m \leqslant 1$) is a constant parameter. In order to implement the above described model into the FE code simulating concrete at elevated temperatures, Relation (10) was extended by replacing the (constant) bubbling pressure $p_{\mathrm{b}}^{\mathrm{c}}$ by a temperature-dependent polynomial function [25,26], yielding (see Fig. 6)[6]

$$S_{\mathrm{w}} = \left[1 + \left(\frac{E_{\mathrm{s}}}{A_{\mathrm{s}}} p^{\mathrm{c}} \right)^{1/(1-m)} \right]^{-m}. \tag{11}$$

4.1.3. Permeability of heated concrete

The dependence of the intrinsic permeability k_{int} (m^2) on temperature was derived from experimental results presented in [2,42] (see Fig. 7). In case of (compressible) gas flow, the absolute permeability k (m^2) (see Eqs. (1)–(3)) is — due to the so-called slip-flow phenomenon-dependent on the gas pressure, reading [43]

$$k = k_{\mathrm{int}} \left(1 + \frac{b}{p^{\mathrm{g}}} \right), \tag{12}$$

where b (Pa) is the so-called slip-flow constant. Within the analyses, $b = 1 \times 10^5$ Pa is considered. In case of (incompressible) water flow, no slip-flow effect exists. Hence, $k = k_{\mathrm{int}}$.

As regards the relative permeability of partially saturated porous media, various models exist. In [30,31], the relative permeability to water is given by [4,30,31]

$$k^{\mathrm{rw}} = \left(\frac{S_{\mathrm{w}} - S_{\mathrm{w}}^{\mathrm{r}}}{1 - S_{\mathrm{w}}^{\mathrm{r}}} \right)^{A_{\mathrm{w}}}, \tag{13}$$

where $S_{\mathrm{w}}^{\mathrm{r}}$, (dimensionless) is the residual saturation (the porous medium cannot be dewatered further) and A_{w} (dimensionless) is a constant parameter. The relative

---

[6]The temperature-dependent parameters in Eq. (11) are defined as

$A_{\mathrm{s}} = p_{\mathrm{b}}^{\mathrm{c}}$ for $T \leqslant 100\,^{\circ}\mathrm{C}$ and
$A_{\mathrm{s}} = B_{\mathrm{s}} + (p_{\mathrm{b}}^{\mathrm{c}} - B_{\mathrm{s}})$

$$\left[2 \left(\frac{T - 100}{T_{\mathrm{crit}} - 100} \right)^3 - 3 \left(\frac{T - 100}{T_{\mathrm{crit}} - 100} \right)^2 + 1 \right]$$

for $T > 100\,^{\circ}\mathrm{C}$,

and

$$E_{\mathrm{s}} = \left(\frac{T_{\mathrm{crit}} - T_0}{T_{\mathrm{crit}} - T} \right)^{N_{\mathrm{s}}} \quad \text{for } T \leqslant (T_{\mathrm{crit}} - Z_{\mathrm{s}}) \text{ and}$$

$$E_{\mathrm{s}} = E_{\mathrm{s},0} \left[\frac{N_{\mathrm{s}}}{Z_{\mathrm{s}}} T + 1 - \frac{N_{\mathrm{s}}}{Z_{\mathrm{s}}} (T_{\mathrm{crit}} - Z_{\mathrm{s}}) \right]$$

for $T > (T_{\mathrm{crit}} - Z_{\mathrm{s}})$,

with

$$E_{\mathrm{s},0} = \left(\frac{T_{\mathrm{crit}} - T_0}{Z_{\mathrm{s}}} \right)^{N_{\mathrm{s}}}.$$

Hereby, B_{s} (Pa), N_{s} (dimensionless), and Z_{s} ($^{\circ}\mathrm{C}$) are constant parameters, with the latter governing the transition over the critical temperature $T_{\mathrm{crit}} = 374.15\,^{\circ}\mathrm{C}$.

Table 1
Properties of lining concrete for the coupled analysis

Input parameter	Initial value (at $T_0 = 20\,°C$)	Temperature dependence	Source
Thermal conductivity, λ [kJ/(h m K)]	6.72	$\lambda = \lambda_0 - 0.006\,(T-T_0)$ for $T < 800\,°C$	[25]
Density, ρ_c (ρ_s) (kg/m^3)	2362	$\rho = \rho_0 + 0.3(T-T_0)$	[33]
Specific heat capacity, c_p [kJ/(kg K)]	0.90	$c_p = c_{p0} + 0.0005(T-T_0)$ for $T < T_{crit} = 374.15\,°C$	[25]
Porosity, n (dimensionless)	0.142	$n = n_0 + 0.0001(T-T_0)$	[39]
Intrinsic permeability, k_{int} of concrete with 0 kg/m^3 PP-fibers (m^2)	1.22×10^{-16}	See Fig. 7	[2]
Intrinsic permeability, k_{int} of concrete with 1.5 kg/m^3 PP-fibers (m^2)	4.58×10^{-16}	See Fig. 7	[2]
Specific enthalpy of vaporization, h (kJ/kg)	2486	$h = 267.2(T_{crit}-T)^{0.38}$ for $T < T_{crit} = 374.15\,°C$	[40]
Specific enthalpy of dehydration, l_ξ^w (kJ/kg)	796	–	[41]

Table 2
Properties of lining concrete and reinforcement for the structural safety assessment

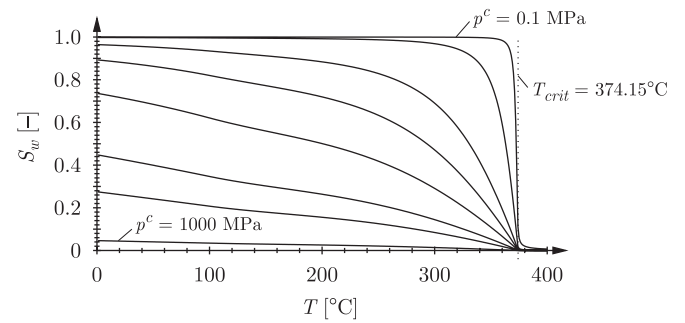| Input parameter	Value
Concrete	
Young's modulus E (MPa)	30,000
Poisson's ratio v (dimensionless)	0.2
Compressive strength f_c (MPa)	30
Tensile strength f_t (MPa)	3
Thermal expansion coefficient α_T (1/°C)	1×10^{-5}
Reinforcing steel	
Young's modulus E (MPa)	210,000
Yield strength f_y (MPa)	500
Thermal expansion coefficient α_T (1/°C)	1.2×10^{-5}

Fig. 6. Degree of saturation versus temperature for different values for the capillary pressure $p^c = 0.1, 1, 5, 10, 20, 50, 100, 1000$ MPa according to Eq. (11) [25,26] (parameters: $p_b^c = 18.624$ MPa, $m = 0.44$, $B_s = 30$ MPa, $N_s = 1.2$, $Z_s = 0.5\,°C$).

4.2. Initial and loading conditions

Within all analyses, the following initial conditions are employed: $T_0 = 20\,°C$, $p_0^g = 101{,}325$ Pa, $p_0^c = 55 \times 10^6$ Pa (giving, according to Eq. (11), an initial degree of saturation of $S_{w0} = 0.40$). The BC at the heated surface are: (i) direct prescription of temperature $\bar{T}$ (see Fig. 9), (ii) direct prescription of the atmospheric pressure $p^{atm} = 101{,}325$ Pa, and (iii) convective mass transfer (with prescribed vapor pressure of the surroundings, with $p_\infty^{gw} = 1020$ Pa, and a convective mass-transfer parameter $\beta_c = 0.025$ m/s). The mentioned BC are prescribed at the top and the bench of the tunnel. Since the invert is protected by additional installations required for the track (see Fig. 4(a)), constant temperature, gas pressure, and capillary pressure are prescribed there.

The history of the prescribed surface temperature $\bar{T}$ (°C) was extracted from large-scale fire experiments [33,44], characterized by exposure of the specimens to temperature loading typical for tunnel fires (see Fig. 9). The applied mechanical loading consisted of (i) self-weight of the lining, with $\rho = 2500$ kg/m^3, and (ii) soil pressure according to the geological situation at the considered cross-section of the tunnel, acting in both vertical and horizontal direction (see [1] for details).
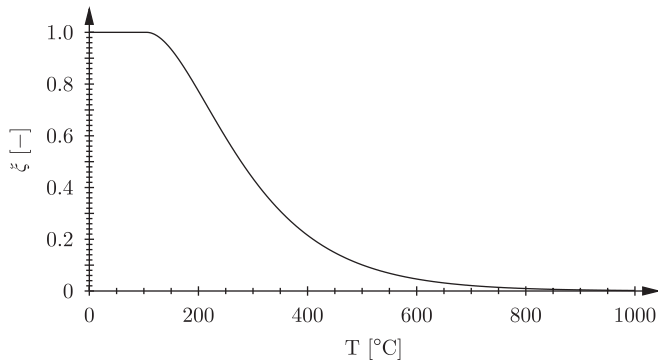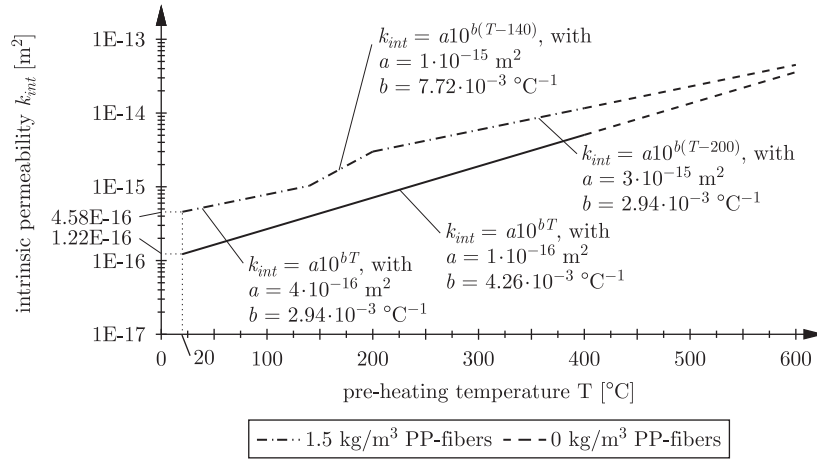

Fig. 5. Degree of hydration versus temperature [25].

permeability to gas is given by [4,31,32]

$$k^{rg} = 1 - \left(\frac{S_w}{S_w^{cr}}\right)^{A_g}, \tag{14}$$

where S_w^{cr} (dimensionless) is the critical saturation (above which no gas flow exists in the porous medium) and A_g (dimensionless) is a constant parameter. Within the numerical analyses, $S_w^r = 0$, $A_w = 6.0$, $S_w^{cr} = 1.0$, and $A_g = 1.0$ (see Fig. 8).

Fig. 7. Approximation of experimental permeability results for concrete with 0 and $1.5\,kg/m^3$ PP-fibers [2,42].
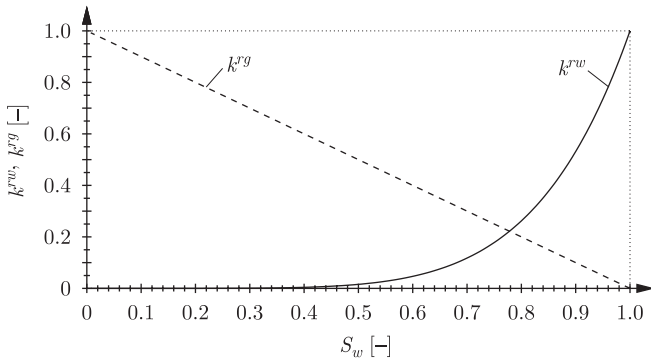

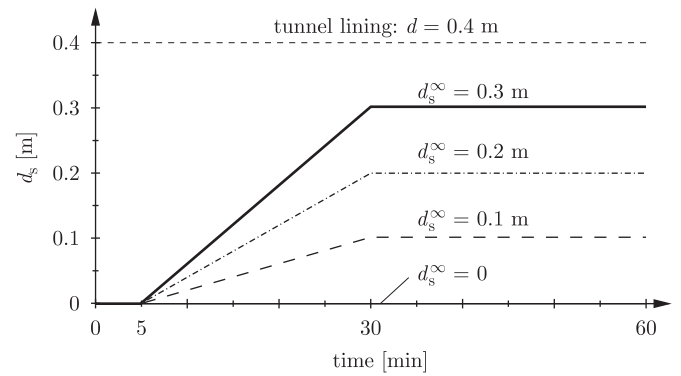Fig. 8. Relative permeabilities to water and gas as a function of saturation [4].

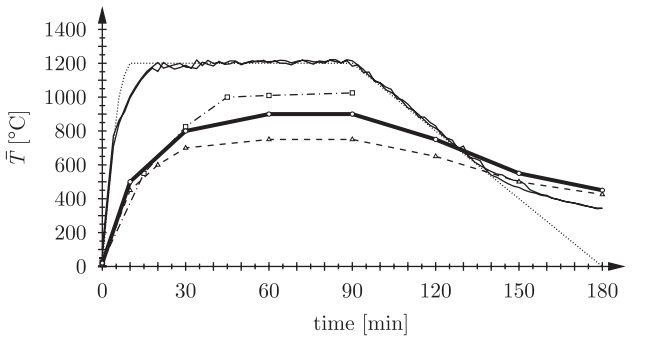Fig. 10. Considered spalling scenarios (derived from experimental observations/data [33]).

Table 3
Analyses performed

Analysis	Temperature distribution obtained from	Compressive strength of concrete
A	Uncoupled thermal analysis	$f_c = f_c(T)$, see Eq. (5)
B	Uncoupled analysis incl. heat sinks	$f_c = f_c(T)$, see Eq. (5)
C	Coupled analysis	$f_c = f_c(T, p)$, see Eq. (6)

Fig. 9. History of the surface temperature extracted from large-scale fire experiments [33,44].

4.3. Results and discussion

Within the analyses, the influence of spalling on the tunnel safety is investigated by prescribing different spalling scenarios (see Fig. 10) which were derived from the fire experiments presented in [33] (spalling was monitored acoustically as well as by means of dynamic acceleration sensors).

Three analyses were performed (see Table 3), characterized by temperature distributions obtained from different analysis schemes (uncoupled analysis, see, e.g., [41,45], or coupled analysis, see Section 2) and by disregard/consideration of the effect of the gas pressure on the compressive strength of concrete (see Fig. 3).

For the case of no spalling ($d_s^\infty = 0$), concrete with and without PP-fibers was compared, indicating an increased spalling risk of concrete without PP-fibers (for details, see [2]), which is in agreement with observations during fire

experiments presented in [33,44]. The uncoupled as well as the coupled analyses give access to temperature distributions for the considered spalling scenarios (see Fig. 11 for $d_s^\infty = 0.2$ m). Spalling results in a faster propagation of the heating front and, therefore, in an increased thermal loading of the remaining tunnel lining, finally giving higher thermal degradation of the cross-section as compared to the analysis with $d_s^\infty = 0$. Comparison of different analyses (Analyses A–C) shows that consideration of heat sinks within the uncoupled analysis (Analysis B) results in lower temperatures compared to the uncoupled thermal analysis (Analysis A). Furthermore, consideration of mass transport within the concrete structure results in cooling of shallow regions, leading to a further decrease of the temperature. In addition, consideration of mass transport results in heating (to a smaller extent) of deeper concrete regions, indicated by a kink in the distribution obtained from Analysis C. Comparison of numerical results with temperature measurements has shown that, even though the prescribed surface temperature follows the experimental temperature history in case of the uncoupled as well as the coupled analysis, the coupled analysis gives more realistic temperature distributions (for details, see [2]).

In contrast to numerical results from the uncoupled analyses (Analyses A and B), the coupled analysis (Analysis C) gives information on quantities related to mass transport. Fig. 12 shows gas-pressure distributions for a final spalling depth of $d_s^\infty = 0.2$ m. Hereby, the plastic mat located between tunnel lining and shotcrete shell (see Section 4.1) is considered either as impermeable layer for water and vapor transport or not (sealed and unsealed conditions, respectively), representing the upper and lower limit, respectively, for the gas pressure. The maximum pressure is apparently not (or only little) affected by the plastic mat at the outer surface of the tunnel lining. The pressure distribution between the location of the maximum pressure and the outer surface, however, varies significantly for $t \geqslant 30$ min, where the gas pressure at the outer surface rises in case the plastic mat is considered as impermeable layer since water and vapor are hindered from escaping at that interface. In case the plastic mat is disregarded, the gas

pressure at the interface between tunnel lining and shotcrete shell remains equal to the atmospheric pressure.

Within the structural analysis, the tunnel safety is monitored by the vertical displacement at the top of the tunnel as well as the level of loading of the circumferential reinforcement. Fig. 13 shows the vertical displacement v (cm) at the top of the tunnel for different spalling scenarios. Hereby, the vertical displacement due to self-weight of the tunnel lining and soil pressure is indicated by v_0. For $d_s^\infty = 0$, v increases gradually until $t = 52$ min resulting from the heat-induced decrease of strength and stiffness of the lining materials, i.e., concrete and steel. With continuation of temperature loading, thermal dilation associated with the continuous heating of the lining results in partial compensation of the temperature-induced displacement. According to Fig. 13, an increasing spalling depth results in an increased compliance of the tunnel structure. During spalling, v increases rapidly, with the maximum displacement observed after the final spalling depth d_s^∞ is reached. With continuation of temperature loading, again parts of the displacement are compensated by thermal dilation of the remaining lining. In no case, collapse of the
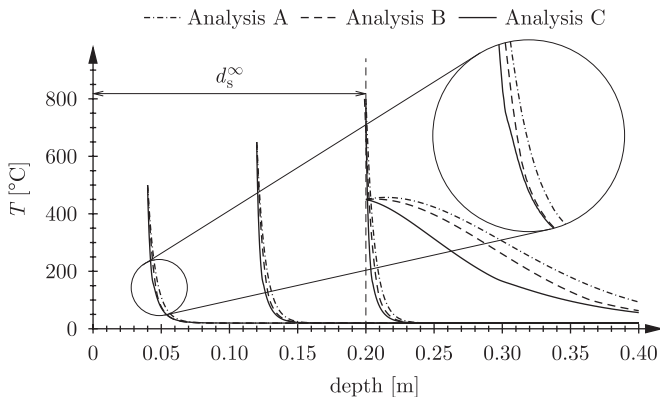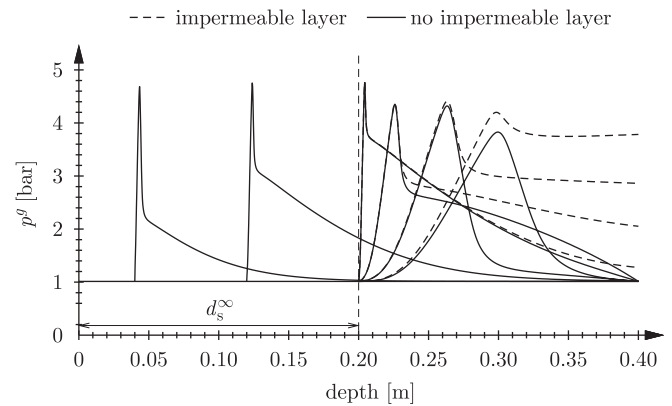

Fig. 12. Gas-pressure distributions obtained from Analysis C with or without consideration of impermeable layer ($d_s^\infty = 0.2$ m, $t = 0$, 10, 20, 30, 40, 90, 180 min).

Fig. 11. Temperature distributions for different analyses ($d_s^\infty = 0.2$ m, $t = 10, 20, 30, 180$ min).
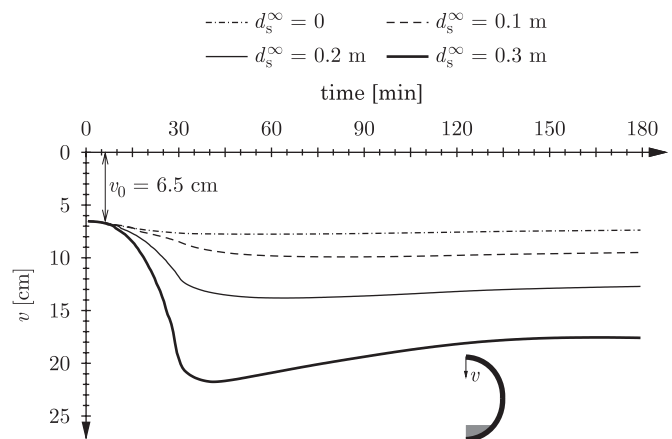

Fig. 13. History of vertical displacement at top of tunnel obtained from Analysis C considering different spalling scenarios (vertical displacement due to self-weight and soil pressure: $v_0 = 6.5$ cm).
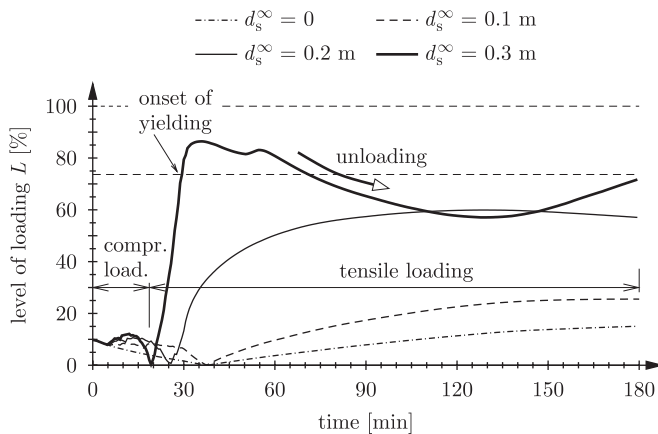
Fig. 14. History of level of loading of the outer circumferential reinforcement at top of tunnel obtained from Analysis C considering different spalling scenarios.
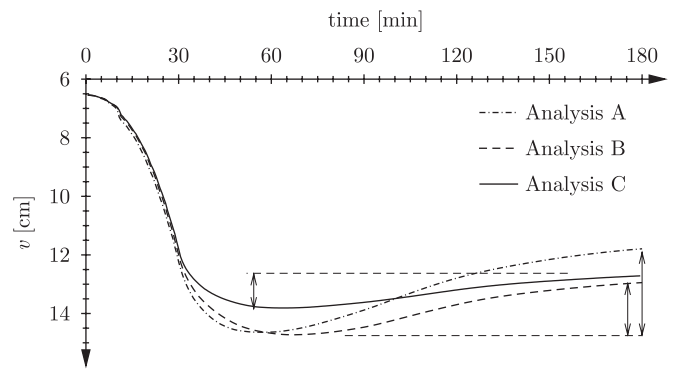

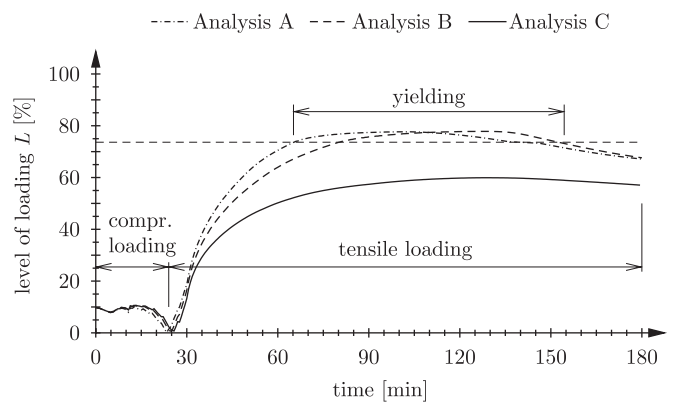Fig. 15. History of vertical displacement at top of tunnel for $d_s^\infty = 0.2$ m (Analyses A–C).

Fig. 16. History of level of loading of the outer circumferential reinforcement at top of tunnel for $d_s^\infty = 0.2$ m (Analyses A–C).

tunnel is observed, which would be indicated by a sharp increase of v.

Fig. 14 shows the level of loading in the outer circumferential reinforcement at the top of the tunnel, defined as [1]

$$L = \frac{|\sigma|}{\max\{\zeta_{RF}(T)\}} = \frac{|\sigma|}{1.1 f_y(T)}, \qquad (15)$$

where σ (MPa) is the actual stress in the reinforcement and f_y (MPa) is the yield strength of the reinforcing steel. Hereby, concrete cracking is modeled by the smeared-crack approach. L equals zero in case of unloaded reinforcement and amounts to 100% when the stress in the reinforcement reaches the maximum possible loading, given by $1.1f_y(T)$ [1]. Application of self-weight and soil pressure on the tunnel structure results in compressive loading of the outer reinforcement due to bending with $L \approx 10\%$. During temperature loading, thermal dilation results in compressive stresses at the heated surface and, therefore in tensile loading of the outer reinforcement, leading to a reduction of the compressive loading and, thus, of the level of loading. When the loading of the reinforcement changes to tensile loading, L increases again. With increasing spalling depth, this shift from compressive to tensile loading occurs earlier in time. Yielding of the reinforcement (starting at $L = 73.6\%$ [1]) is observed for the analysis with $d_s^\infty = 0.3$ m. As opposed to the other spalling scenarios, unloading of the outer reinforcement is observed after $t = 36$ min in case of $d_s^\infty = 0.3$ m, which corresponds to the time instant at which the maximum displacement is reached (see Fig. 13). This unloading is associated with thermal dilation (causing compensation of parts of the vertical displacement), resulting in compressive stresses close to the heated surface and tensile stresses at the outside. In case of $d_s^\infty = 0.3$ m, the outer reinforcement is located closer to the middle surface of the remaining lining after spalling has finished compared to the other considered spalling scenarios, explaining the observed unloading of the

reinforcement. As temperature loading continues, L increases in consequence of the continuous reduction of $f_y(T)$ (see Eq. (15)). Until the end of fire loading, however, no further yielding is observed for $d_s^\infty = 0.3$ m. For all spalling scenarios and considering the fire loading depicted in Fig. 9, the level of loading never reached 100%, indicating some remaining load-carrying capacity.

The results obtained from Analyses A to C are compared in Figs. 15 and 16, showing little difference until the end of spalling. Thereafter, the higher temperatures within the tunnel lining in case of Analyses A and B result in more thermal degradation of the cross-section and, therefore, in larger displacements (see Fig. 15). The lower (more realistic) temperature loading considered in Analysis C leads to smaller maximum displacements. With continuation of fire loading, the compensation of displacement by the continuous heating of the remaining part of the lining is the highest for Analysis A.

As regards the level of loading L (see Fig. 16), yielding of the outer circumferential reinforcement is observed only for Analyses A and B. As the temperature loading continues, L decreases and plastic loading of the reinforcement, characterized by $L > 73.6\%$, stops. For Analysis C, the lower temperature loading results in $L < 73.6\%$, hence, no yielding of the reinforcement is observed.

5. Conclusions and outlook

In this paper, a fully coupled thermo-hydro-chemical model simulating the governing transport processes in heated concrete and a structural safety assessment tool [1] were combined within a two-step analysis scheme. Within the numerical model, the influence of temperature and gas pressure on the stress and deformation state were taken into account. The analysis tool was used to investigate the structural performance of a tunnel cross-section characterized by low overburden subjected to fire loading and different spalling scenarios.

The results obtained from the coupled analysis of heat and mass transport in heated concrete led to the following conclusions:

- Comparing the gas-pressure distributions for concrete with and without polypropylene (PP) fibers indicates that the lower permeability in case of concrete without PP-fibers results in higher gas pressures and, therefore, leads to an increased spalling risk (for details, the reader is referred to [2]). This is in agreement with observations during fire experiments presented in [33,44].
- Investigation of different spalling scenarios within the analyses showed that the thermal loading and, therefore, the thermal degradation of the remaining lining is higher for increasing spalling depths.
- Consideration of mass transport within the coupled analysis led to lower thermal loading of the tunnel lining compared to the uncoupled thermal analysis either with or without consideration of heat sinks associated with evaporation of water and dehydration of the cement paste. Hence, the thermal degradation of the cross-section is lower in case the (more realistic) temperature distributions from the coupled analysis are considered.

Within the structural safety assessment, the temperature and gas-pressure distributions taken either from the uncoupled or the coupled analyses served as input into the numerical model. The results obtained from the structural analyses led to the following conclusions:

- With increasing spalling depth, the compliance of the tunnel structure as well as the level of loading in the outer circumferential reinforcement increased. This resulted in increased vertical displacement at the top of the tunnel with increasing spalling depth.
- Considering different analyses showed that the lower (and more realistic) temperature distributions obtained from the coupled analyses led to a smaller compliance of the tunnel structure and, therefore, to smaller displacements. With continuation of temperature loading, on the other hand, the lower thermal loading yielded less compensation of vertical displacement due to thermal dilation.
- None of the considered spalling scenarios led to collapse of the tunnel structure for the considered temperature

loading, even though a reduction of the lining thickness by 75% due to spalling was considered. In case no collapse of the tunnel is indicated by the numerical analysis, the results allow:

(1) estimation of the safety level of the tunnel structure during as well as after fire loading, which is important for rescue forces as well as the engineer or the tunnel owner, and

(2) determination of the necessary amount of repair measures (e.g., lining thickness that has to be replaced), leading to an estimation of the repair costs after a tunnel fire.

Within the structural model, layered shell elements, considering a tunnel of 1 m length, are used. Hence, the extension of the employed analysis model to the third dimension in order to consider 3D structural effects and the longitudinal variation of temperature loading, is straightforward. The functions describing the temperature dependence of the material parameters for concrete and steel were taken from national and international standards and represent empirical material functions derived from experimental data. In order to improve the underlying functions, multi-scale models on basis of a micromechanics approach (see, e.g., [46,47]) for the description of material parameters of concrete and steel under elevated temperatures are currently developed. So far, the effect of the gas pressure on the structural performance of the tunnel lining was considered by reducing the in-plane compressive strength of concrete. Hereby, the gas pressure was transformed into an equivalent out-of-plane tensile stress. In future work, this equivalent stress shall be combined with the in-plane restrained thermal stresses allowing us to determine the spalling history as a function of gas-pressure, stress state, and temperature distribution instead of prescribing a spalling history derived from experiments. This will allow for combination of the yet-separated parts of the two-step analysis scheme for the safety assessment of structures subjected to fire load.

References

[1] Savov K, Lackner R, Mang HA. Stability assessment of shallow tunnels subjected to fire load. Fire Safety J 2005;40:745–63.

[2] Zeiml M, Leithner D, Lackner R, Mang HA. How do polypropylene fibers improve the spalling behavior of in-situ concrete? Cement Concrete Res 2006;36(5):929–42.

[3] Lewis R, Schrefler B. The finite element method in the static and dynamic deformation and consolidation of porous media. 2nd ed. Chichester: Wiley; 1998.

[4] Gawin D, Majorana CE, Schrefler BA. Numerical analysis of hygro-thermal behaviour and damage of concrete at high temperature. Mech Cohes-Frict Mater 1999;4:37–74.

[5] Schrefler BA. Mechanics and thermodynamics of saturated/unsaturated porous materials and quantitative solutions. Appl Mech Rev (ASME) 2002;55(4):351–88.

[6] Gawin D, Pesavento F, Schrefler BA. Modelling of hygro-thermal behaviour of concrete at high temperature with thermo-chemical and mechanical material degradation. Comput Methods Appl Mech Eng 2003;192:1731–71.

[7] Schrefler BA. Multiphase flow in deforming porous material. Int J Numer Methods in Eng 2004;60:27–50.

[8] Consolazio GR, McVay MC, Rish III JW. Measurement and prediction of pore pressure in cement mortar subjected to elevated temperature. In: Phan LT, Carino NJ, Duthinh D, Garboczi E, editors. Proceedings of the international workshop on fire performance of high-strength concrete. Gaithersburg, MD: NIST; 1997. p. 125–48.

[9] Consolazio GR, Chung JH. Numeric simulation of near-surface moisture migration and stress development in concrete exposed to fire. Comput Concrete 2004;1(1):31–46.

[10] Lien H-P, Wittmann FH. Mass transfer in inhomogeneous porous media under thermal gradients. Nucl Eng Des 1998;179:179–89.

[11] Tenchev R, Li L, Purkiss J. Finite element analysis of coupled heat and moisture transfer in concrete subjected to fire. Numer Heat Transfer 2001;39:685–710.

[12] Ahmed G, Hurst J. An analytical approach for investigating the causes of spalling of high-strength concrete at elevated temperatures. In: Phan LT, Carino NJ, Duthinh D, Garboczi E, editors. Proceedings of the international workshop on fire performance of high-strength concrete. Gaithersburg, MD: NIST; 1997. p. 95–108.

[13] Ahmed G, Hurst J. Coupled heat and mass transport phenomena in siliceous aggregate concrete slabs subjected to fire. Fire Mater 1997;21(4):161–8.

[14] Bažant ZP, Thonguthai W. Pore pressure and drying of concrete at high temperature. J Eng Mech Div 1978;104:1059–79.

[15] Bažant ZP. Analysis of pore pressure, thermal stress and fracture in rapidly heated concrete. In: Phan LT, Carino NJ, Duthinh D, Garboczi E, editors. Proceedings of the international workshop on fire performance of high-strength concrete. Gaithersburg, MD: NIST; 1997. p. 155–64.

[16] Bažant Z, Zi G. Decontamination of radionuclides from concrete by microwave heating. I: theory. J Eng Mech (ASCE) 2003;129(7):777–84.

[17] Zi G, Bažant Z. Decontamination of radionuclides from concrete by microwave heating. II: computations. J Eng Mech (ASCE) 2003; 129(7):785–92.

[18] Richter E, Hosser D. Baulicher Brandschutz bei Verkehrstunneln in offener Bauweise [Fire protection for tunnels]. Beton Stahlbetonbau 2002;97(4):178–84 [in German].

[19] Wageneder J. Traglastuntersuchungen unter Brandeinwirkungen [Ultimate-load investigations considering fire load]. Bauingenieur 2002;77:184–92 [in German].

[20] El-Arabi I, Duddeck H, Ahrens H. Structural analysis for tunnels exposed to fire temperatures. Tunneling Underground Space Technol 1992;7(1):19–24.

[21] Schrefler BA, Brunello P, Gawin D, Majorana CE, Pesavento F. Concrete at high temperature with application to tunnel fire. Comput Mech 2002;29:43–51.

[22] Pichler C, Lackner R, Mang HA. Safety assessment of concrete tunnel linings under fire load. J Struct Eng (ASCE) 2006;132(6): 961–9.

[23] Ahmed K. Numerical modelling of tunnel lining at high temperature using sandwich element. PhD thesis, University of Innsbruck, Innsbruck, Austria, 2004.

[24] Harmathy T, Allen L. Thermal properties of selected masonry unit concretes. ACI J 1973;70(2):132–42.

[25] Pesavento F. Nonlinear modelling of concrete as multiphase porous material in high temperature conditions. PhD thesis, University of Padua, Padua, Italy, 2000.

[26] Giannuzzi G. Centro Ricerche Energia Casaccia-ENEA, Rome, Italy, 2000, Private communications.

[27] van Genuchten MT, Nielsen DR. On describing and predicting the hydraulic properties of unsaturated soils. Ann Geophys 1985;3(5): 615–27.

[28] Baroghel-Bouny V, Mainguy M, Lassabatere T, Coussy O. Characterization and identification of equilibrium and transfer moisture properties for ordinary and high-performance cementitious materials. Cement Concrete Res 1999;29:1225–38.

[29] Monlouis-Bonnaire JP, Verdier J, Perrin B. Prediction of the relative permeability to gas flow of cement-based materials. Cement Concrete Res 2004;34(5):737–44.

[30] Scheidegger A. The physics of flow through porous media. 3rd ed. Toronto: University of Toronto Press; 1974.

[31] Bear J. Dynamics of fluids in porous media. New York: Dover; 1988.

[32] Thomas H, Sansom M. Fully coupled analysis of heat, moisture, and air transfer in unsaturated soil. J Eng Mech (ASCE) 1995;121(3): 392–405.

[33] Kusterle W, Lindlbauer W, Hampejs G, Heel A, Donauer P-F, Zeiml M, et al. Brandbestandigkeit von Faser-, Stahl- und Spannbeton [Fire resistance of fiber-reinforced, reinforced, and prestressed concrete]. Technical Report 544, Bundesministerium für Verkehr, Innovation und Technologie, Vienna, 2004 [in German].

[34] Duddeck H. Guidelines for the design of tunnels. Tunneling and Underground Space Technology 1988;3(3):237–49.

[35] Wissmann W. Zur statischen Berechnung beliebig geformter Stollen- und Tunnelauskleidungen mit Hilfe von Stabwerkprogrammen [On static analysis of arbitrarily formed linings of mines and tunnels using computer programs for beam structures]. Der Bauing 1968;43(1):1–8 [in German].

[36] CEB. Fire design of concrete structures, Bulletin d'Information 208, CEB, Lausanne, Switzerland, 1991.

[37] European Committee for Standardization (CEN). Eurocode 2-Bemessung und Konstruktion von Stahlbeton- und Spannbetontragwerken — Teil 1–2: Allgemeine Regeln — Tragwerksbemessung fur den Brandfall [Eurocode 2 — design of concrete structures — Parts 1–2: general rules — structural fire design], 2004 [in German].

[38] Chateau X, Dormieux L. Micromechanics of saturated and unsaturated porous media. Int J Numer Anal Methods Geomech 2002;26:831–44.

[39] Kalifa P, Menneteau F-D, Quenard D. Spalling and pore pressure in HPC at high temperatures. Cement Concrete Res 2000;30: 1915–27.

[40] Blanke W, Biermann M. Thermophysikalische Stoffgrößen [Thermophysical material parameters], vol. 1. Berlin: Springer; 1989 [in German].

[41] Zeiml M. Analytical and numerical modeling of heat and water-vapor transport in concrete subjected to fire loading. Master's thesis, Vienna University of Technology, Vienna, Austria, 2004.

[42] Zeiml M, Lackner R, Leithner D, Eberhardsteiner J. Identification of gas-transport properties of concrete subjected to high temperature. Cement Concrete Res; 2007, submitted for publication.

[43] Klinkenberg LJ. The permeability of porous media to liquids and gases, American Petroleum Institute, Drilling Production Practice 1941:200–13.

[44] Horvath J. Beitrage zum Brandverhalten von Hochleistungsbeton [Contributions to the behavior of high-performance concrete under

fire], PhD thesis, Vienna University of Technology, Vienna, Austria, 2003 [in German].

[45] Zeiml M, Lackner R, Mang HA. Coupled analysis of heat and multiphase mass transport in concrete subjected to fire loading. In: Papadrakakis M, Onate E, Schrefler B, editors. CD-ROM proceedings of the international conference on computational methods for coupled problems in science and engineering (Coupled Problems 2005). Barcelona: CIMNE; 2005. 23 pp.

[46] Ulm F-J, DeJong M. Sources of high temperature degradation of cement-based materials: nanoindentation and microporoelastic analysis. Technical Report CEE Report R05-01, Department of Civil and Environmental Engineering, Massachusetts Institute of Technology, Cambridge, USA, 2005.

[47] DeJong M, Ulm F-J. The nanogranular behavior of C-S-H at elevated temperatures (up to 700 °C). Cement Concrete Res 2007;37(1):1–12.